Signatures of Multiband Effects in High-Harmonic Generation in Monolayer MoS_2

Lun Yue,[1] Richard Hollinger,[2,3,*] Can B. Uzundal,[2,3] Bailey Nebgen,[2,3] Ziyang Gan,[4] Emad Najafidehaghani,[4] Antony George,[4] Christian Spielmann,[5,6,7] Daniil Kartashov,[5,6] Andrey Turchanin,[4,6] Diana Y. Qiu,[8] Mette B. Gaarde,[1] and Michael Zuerch[2,3,5,†]

[1]*Department of Physics and Astronomy, Louisiana State University, Baton Rouge, Louisiana 70803, USA*
[2]*Department of Chemistry, University of California, Berkeley, California 94720, USA*
[3]*Lawrence Berkeley National Laboratory, Materials Sciences Division, Berkeley, California 94720, USA*
[4]*Institute of Physical Chemistry, Friedrich Schiller University Jena, 07743 Jena, Germany*
[5]*Institute of Optics and Quantum Electronics, Friedrich Schiller University Jena, 07743 Jena, Germany*
[6]*Abbe Center of Photonics, Friedrich Schiller University Jena, 07745 Jena, Germany*
[7]*Helmholtz Institute Jena, 07743 Jena, Germany*
[8]*Department of Mechanical Engineering and Materials Science, Yale University, New Haven, Connecticut 06520, USA*

(Received 14 January 2022; revised 8 April 2022; accepted 7 September 2022; published 28 September 2022)

High-harmonic generation (HHG) in solids has been touted as a way to probe ultrafast dynamics and crystal symmetries in condensed matter systems. Here, we investigate the polarization properties of high-order harmonics generated in monolayer MoS_2, as a function of crystal orientation relative to the mid-infrared laser field polarization. At several different laser wavelengths we experimentally observe a prominent angular shift of the parallel-polarized odd harmonics for energies above approximately 3.5 eV, and our calculations indicate that this shift originates in subtle differences in the recombination dipole strengths involving multiple conduction bands. This observation is material specific and is in addition to the angular dependence imposed by the dynamical symmetry properties of the crystal interacting with the laser field, and may pave the way for probing the vectorial character of multiband recombination dipoles.

DOI: 10.1103/PhysRevLett.129.147401

High-harmonic generation (HHG) from intense laser pulses in solids is increasingly attracting attention as a probe of ultrafast electronic processes in solids [1–3]. HHG spectroscopy in condensed matter has been used to investigate phase transitions [4] as well as quantum phenomena like the Berry curvature [5,6], electron correlation in the condensed phase [7–10], and topological surface states [11–13]. Solid-state HHG results from carrier dynamics following the excitation of electrons in the strong field of a laser pulse, and originates from both a nonlinear intraband current and, in case of recombination at high kinetic energies, an interband polarization [14–16]. HHG from atomically thin semiconductors such as some of the transition metal dichalcogenides (TMDs) has gained special interest [5,17–22]. In addition to their interesting fundamental properties and their potential applications for optoelectronics and spintronics [23], TMDs are ideal for investigating the microscopic origin of HHG due to the absence of laser propagation effects in the material [15,24,25].

The characteristics of the harmonic emission depend critically on the combined temporal translation symmetry of the laser field and the spatial symmetry of the system, referred to as the dynamical symmetry (DS) [26]. An example well known from gas-phase HHG is the absence of the emission of even-order harmonics in centrosymmetric systems driven by linearly polarized lasers. In crystalline systems, the presence of multiple spatial symmetry elements has major consequences for the harmonic selection rules and polarization states [27–30]. For example, it was shown in the TMD MoS_2 that even-order harmonics are polarized perpendicularly when the driving laser is polarized along the zigzag direction [5,17]. In addition to the crystal symmetry properties, material-specific properties can also strongly affect harmonic characteristics, since different band structures and dispersion relations will give rise to different carrier dynamics. For example, it was recently demonstrated that the polarization properties of HHG can deviate in different TMDs [21], even though they in principle should obey the same dynamical symmetry selection rules. The understanding of the interplay between the symmetry- and material-specific properties in HHG is crucial to the probing of material-specific properties such as band structures [31] and the vectorial character of the transition dipoles [32]. Accurate extraction of such material properties based on measurement of solid-state HHG spectra will allow leveraging of the available femtosecond time resolution of solid-state HHG spectroscopy to trace, e.g., phase transitions in materials [4].

While much of the microscopic HHG dynamics can be understood in terms of a two-band picture [14,16,17,21,32–34] involving a filled valence band and a single conduction

band, a number of works have highlighted the role of multiple bands [19,35–39]. In particular, it has been experimentally demonstrated that multiple bands were responsible for nonintuitive harmonic waveforms in bulk GaSe [40], the emergence of multiple plateaus in rare-gas solids [41], and yield enhancement of different harmonic regions in MgO [42]. In this respect, the observation and understanding of multiband effects in HHG from TMDs is of fundamental interest, and can potentially lead to the ultrafast probing of the complex dynamics leading to HHG, such as electron-hole recombinations from different valence and conduction bands, as well as using HHG to probe dynamic material properties that imprint at higher energies such as hot electron injection in a heterostructure.

In this Letter, in a joint experimental and theoretical effort, we investigate the polarization properties of HHG in monolayer MoS_2, as a function of crystal orientation relative to the mid-infrared (MIR) laser polarization. The DSs of the crystal combined with the temporal translation symmetries of the laser field impose clear constraints on the harmonic emissions and lead to pronounced nodes in the HHG spectra at certain crystal orientations. In addition to the constraints and selection rules imposed by the DSs, we find an angular shift such that for several MIR wavelengths, the parallel-polarized odd-order harmonics below (above) 3.5 eV are enhanced for driver polarization along the armchair (zigzag) direction. By solving the time-dependent density matrix (TDDM) equations involving a valence band and two conduction bands, we trace these angular shifts to electron-hole recombinations from different conduction bands, effectively probing the vectorial nature of recombination dipoles in different bands. Our Letter reveals that electron-hole recombinations from different conduction bands are directly imprinted on the orientation-dependent HHG spectra, and opens up the possibility of probing electron-hole dynamics from multiple recombination pathways.

HHG experiments were performed with MIR laser pulses having wavelength between 3 and 5 μm with full polarization control reaching 1.5 $\mathrm{TW/cm^2}$ in the focus. All experiments were performed at ambient conditions. Monolayer single crystals of MoS_2 were grown on a SiO_2/Si substrate by chemical vapor deposition [43,44] and transferred on to a double side polished c-plane oriented sapphire substrate using a PMMA assisted transfer protocol [43]. The MoS_2 monolayer crystals were characterized by optical microscopy, atomic force microscopy, and Raman spectroscopy [45]. More details on the experimental setup are given in the Supplemental Material (SM) [46]. The 1H-semiconducting phase of the MoS_2 sample was confirmed by investigating the HHG signal from a circular polarized laser and finding that only the $3n \pm 1$ harmonic orders were generated [47].

We show the measured harmonic emission from monolayer MoS_2 in Fig. 1, using three different fundamental

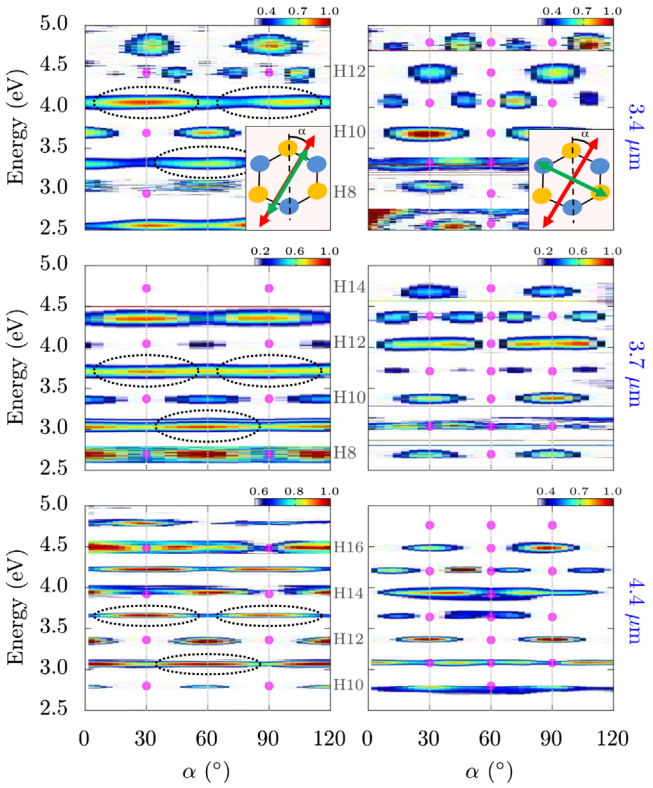

FIG. 1. Experimental HHG spectra measured in the parallel (left column) and perpendicular configuration (right column) for MoS_2 irradiated by intense MIR pulses of central wavelength 3.4 μm (top row), 3.7 μm (middle row), and 4.4 μm (bottom row). Yields are plotted in linear scale and arbitrary units. In the insets, the two polarizer and analyzer configurations are sketched, with α being the angle between the crystal mirror plane and the laser polarization (red arrow), and the polarizer direction indicated by the green arrow. The magenta bullets mark the nodes predicted by a DS analysis, and the dashed ellipses mark the angular shifts of the parallel odd harmonics.

laser wavelengths: 3.4, 3.7, and 4.4 μm. The configurations in which we detect harmonics (green arrows) polarized parallel or perpendicular to the laser polarization (red arrows) are sketched in the insets. We denote α as the angle between the laser polarization and the crystal mirror plane, and for notational convenience label the Γ-M (armchair) direction as $\alpha_0 \equiv n60°$ and the Γ-K (zigzag) direction as $\alpha_{30} \equiv 30° + n60°$, with n being an integer. In Fig. 1, the detected harmonic yields in the two configurations (columns) for different wavelengths (rows) are plotted as a function of harmonic energy and α [48].

Figure 1 illustrates in detail the interplay between DS constraints and material-specific properties and how they manifest on the harmonic emission. There are three notable features: First, the DS constraints give rise to characteristic nodes (magenta bullets) in the angular dependence of both the parallel- and the perpendicular-polarized harmonics, which we will discuss in more detail below. Second, the odd harmonics in the parallel configuration exhibit a

characteristic shift in their angular dependence (angular shift), in which their yields peak at α_0 (α_{30}) for energies below (above) ~3.5 eV. This shift is marked by the dashed ellipses. Third, we find additional minima in the angular dependence of the high energy (~4.5 eV), even harmonics in the parallel configuration for 3.4 μm and 4.4 μm that are not imposed by the DS constraints.

We begin with an analysis of the DSs, which consist of combinations of time and spatial symmetries that leave the time-dependent Hamiltonian invariant [26]. For the spatial symmetries, we can consider the spatial point group C_{3v} instead of the full MoS_2 group D_{3h}, since the laser field is polarized in the MoS_2 (001) plane. We consider linearly polarized monochromatic laser fields that satisfy the time symmetry $\hat{\tau}_2\mathbf{F}(t) = -\mathbf{F}(t)$, where $\hat{\tau}_2$ is an operator that performs a half-cycle time translation. For a laser polarized along α_0, taken as the y axis for convenience, the reflection $\hat{\sigma}^y$ in the y axis is a DS operation. The harmonic yield is contained in the Fourier components $\mathbf{r}_n$ of the time-dependent polarization $\mathbf{r}(t) \equiv \langle\psi(t)|\mathbf{r}|\psi(t)\rangle$. The invariance of $\mathbf{r}(t)$ under the DS operation [13,26] leads to the constraints $(-r_{n,x}, r_{n,y}) = (r_{n,x}, r_{n,y})$, which gives the selection rule that perpendicular harmonics are forbidden along α_0. Similarly, for a laser polarized along α_{30}, taken now as the x axis for convenience, the reflection together with the half-cycle translation of the pulse, $\hat{\sigma}^y\hat{\tau}_2$, constitutes a DS, which leads to the constraints $(-r_{n,x}, r_{n,y})e^{in\pi} = (r_{n,x}, r_{n,y})$ implying the selection rules that parallel even harmonics and perpendicular odd harmonics are forbidden for α_{30}.

The predictions from the DS analysis in Fig. 1 are in clear agreement with the experimental results for all driver wavelengths (to within our signal-noise ratio), illustrating the strength of a general DS analysis and how it may enable the probing of the crystal structure for a known laser field, or the characterization of the field for a known crystal structure. Notably, the nodes implied by DS agree with the perpendicular odd harmonics having the unintuitive 30° periodicity that at first glance deviates from the hexagonal lattice structure of MoS_2. Note that a similar 30° periodicity was recently experimentally observed in GaSe [49] and the topological insulator $BiSbTeSe_2$ [11], with the origin explained purely in terms of the intraband harmonic generation mechanism. This explanation, however, cannot be applied here since our observed above-gap harmonics in MoS_2 (gap 1.8 eV) are predominantly generated by the interband mechanism [17,18]. Finally, as mentioned above, the results in Fig. 1 also demonstrate features that go beyond the DS symmetry, such as the angular shift, which we now will discuss.

We first note that the angular shifts in Fig. 1 manifest near the same harmonic energy for all three laser wavelengths, strongly indicating that they are due to material-specific properties such as the band structure and dipole matrix elements. To shed light onto the origin of these

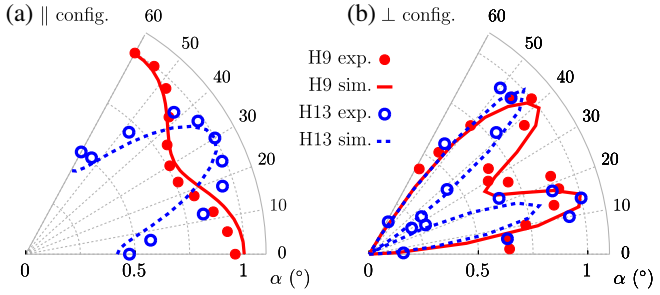

FIG. 2. Experimental and simulation α-dependent HHG yields with a 3.7 μm driver, for the (a) parallel and (b) perpendicular configurations. The yields are normalized to the maximum.

shifts, we proceed by solving the TDDM equations in the velocity gauge and Bloch basis. We employ a linearly polarized field with cosine-squared envelope, full width at half maximum of 99 fs, wavelength 3.7 μm, and peak vector potential $A_0 = 0.168$ atomic units (a.u.) [50]. During the time propagation, we transform to an adiabatic basis [51], to obtain the dressed density matrix elements $\tilde{\rho}^{\mathbf{k}}_{mn}(t)$ and the dressed momentum matrix elements $\tilde{\mathbf{p}}^{\mathbf{k}}_{mn}(t)$, where the subscripts refer to the band indices and $\mathbf{k}$ is the crystal momentum. This procedure allows us to include a phenomenological dephasing time (taken as 10 fs) and to decompose the current into an intraband and interband part. We note that this yields results in agreement with those of the popular multiband semiconductor Bloch equations [52,53], but has the advantage that a periodic gauge [51,54,55] is not required. A different dephasing time slightly changes the α-dependent yield (see SM [46]), but does not influence the conclusions drawn here. To model monolayer MoS_2, we employ the tight-binding model of Refs. [19,56], which takes into account the Mo d_{z^2}, d_{xy}, and $d_{x^2-y^2}$ orbitals with third-nearest hoppings, and results in one valence band (VB) and two conduction bands (CB1 and CB2). The momentum matrix elements are calculated following Ref. [57]. For more details on the theory, see the SM [46].

Figure 2 depicts a comparison of measured and calculated angular yields [58] for harmonic 9 (H9) and H13 in the parallel [Fig. 2(a)] and perpendicular [Fig. 2(b)] configurations for the 3.7 μm driver. The simulations reproduce the angular shift in the parallel configuration and the 30° periodicity in the perpendicular configuration, as well as the overall depth of the modulations. As discussed above, the 30° periodicity can be understood from the DS analysis. However, the DSs do not restrict the parallel odd harmonics, such that emissions for all polarization angles α are in principle allowed. We now investigate the observed angular shift.

The H9 and H13 are emitted above the band edge of MoS_2 (~H5) and originate in the interband currents. The interband harmonic emission process can be interpreted in terms of the recollision model [14,59], and are sketched in

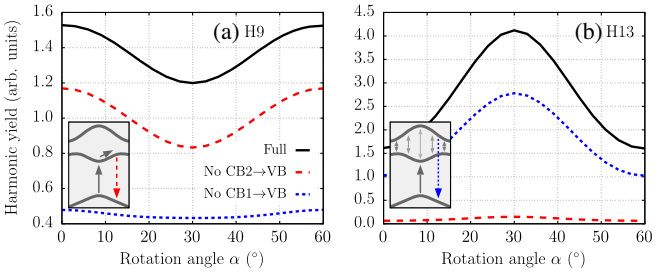

FIG. 3. Simulated harmonic yields as a function of α, for the parallel-polarized (a) H9 and (b) H13. The full (black) curves are the full calculations, the dashed (red) curves are for calculations with $\tilde{\mathbf{p}}^{\mathbf{k}}_{13} = \mathbf{0}$, and the dotted (blue) curves are with $\tilde{\mathbf{p}}^{\mathbf{k}}_{12} = \mathbf{0}$. The insets show sketches of the dominating pathways for generating H9 and H13 (see text).

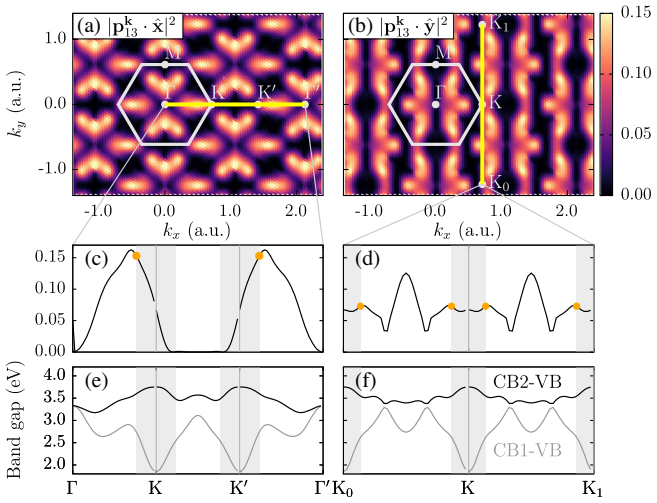

FIG. 4. Modulus squares of the recombination dipoles along (a) $\hat{\mathbf{x}}$ ($\alpha = 30°$) and (b) $\hat{\mathbf{y}}$ ($\alpha = 0°$) directions in a.u. The gray hexagon traces the first Brillouin zone. Panels (c) and (d) plot the same as (a) and (b), but along paths in reciprocal space marked by the yellow lines. Panel (e) and (f) show the band gaps along these paths, with the gray (black) curve between CB1 (CB2) and the VB. The areas marked by gray indicate regions accessible by electron-hole pairs created at the K point, with maximum excursions $\pm A_0$, and the orange dots in (c) and (d) highlight the maximum values in these regions.

the insets of Fig. 3: first, an electron-hole pair is created by tunnel excitation of an electron from the VB to CB1 near the minimum band gap at K; the electron-hole pair is propagated in their respective bands following the acceleration theorem $\mathbf{k} + \mathbf{A}(t)$ [60], and during propagation, the coupling between CB1 and CB2 can lead to electron excitation to CB2 [42]; finally, the electron and hole can coherently recombine either from CB1 or CB2 to the VB, with a probability amplitude weighted by the recombination dipoles, and the harmonic energy given by the band gap at the time of recombination.

We consider the three steps of the recollision process, and discuss the differences between α_0 and α_{30}. First, it should be noted that the populations in the conduction bands at the end of the calculations are very similar: 1.33% in CB1 and 0.84% in CB2 for α_0; and 1.32% in CB1 and 0.86% in CB2 for α_{30}. This means that the initial excitation step cannot be responsible for the HHG yields between α_0 and α_{30} in Figs. 2(a) and 2(b). Since the band dispersions near the K valley in the range $K \pm A_0$ are similar for the two conduction bands, the propagation step appears to play a minor role. This suggests that the angular shift is dominated by the recombination dipole which can be modeled further.

The full black curves in Fig. 3 show the full simulations results, where the parallel polarized H9 in Fig. 3(a) peaks at α_0 and H13 in Fig. 3(b) peaks at α_{30}. The dashed (red) curves are results using $\tilde{\mathbf{p}}^{\mathbf{k}}_{13}(t) = \mathbf{0}$ in the calculations of the interband current, i.e., restricting the CB2 → VB recombination pathway, resulting in a yield almost exclusively from the CB1 → VB pathway. Similarly, the dotted (blue) curves are with $\tilde{\mathbf{p}}^{\mathbf{k}}_{12}(t) = \mathbf{0}$, corresponding to the CB2 → VB recombinations. The H9 yield in Fig. 3(a) is seen to be dominated by recombination from CB1, while the H13 yield in Fig. 3(b) is dominated by recombinations from CB2. Clearly, the α dependence of the yield originates in different characters of of the recombination dipoles $\tilde{\mathbf{p}}^{\mathbf{k}}_{12}(t)$ and $\tilde{\mathbf{p}}^{\mathbf{k}}_{13}(t)$, which we now investigate further.

We choose to focus on the pronounced case, i.e., the bell shape of H13 in Fig. 3(b) with maximum at α_{30} and minimum at α_0 dominated by the CB2 → VB pathway. The recombination matrix elements responsible for the parallel harmonics are proportional to $\mathbf{p}^{\mathbf{k}}_{13} \cdot \hat{\mathbf{e}}_\alpha$, where $\hat{\mathbf{e}}_\alpha$ is a unit vector along α. In Fig. 4, we plot $|\mathbf{p}^{\mathbf{k}}_{13} \cdot \hat{\mathbf{e}}_\alpha|^2$ for α_{30} ($\hat{\mathbf{e}}_\alpha \equiv \hat{\mathbf{x}}$) in (a) and for α_0 ($\hat{\mathbf{e}}_\alpha \equiv \hat{\mathbf{y}}$) in (b). The values along relevant paths in reciprocal space, indicated by the yellow lineouts in Figs. 4(a) and 4(b), are shown in Figs. 4(c) and 4(d), respectively. An electron-hole pair created at K at the zeros of the vector potential will have the maximal excursion $K \pm A_0\hat{\mathbf{e}}_\alpha$ in reciprocal space, which is marked by the gray regions in Figs. 4(c) and 4(d). The maxima in the gray regions are shown by the orange dots, with the values 0.153 for α_{30} and 0.073 for α_0. The ratio between them is 2.10, which is qualitatively in agreement with 2.55—the ratio between the yields at α_{30} and α_0 for the black curve in Fig. 3(b). This suggests that the angular shift is due to the structure of recombination dipoles between the CBs and the VB, with the CB1 → VB recombination dominating the H9 and the CB2 → VB recombination dominating the H13. These considerations are further supported by considering the $\mathbf{k}$-dependent band gaps in Figs. 4(e) and 4(f), where it is observed that the recombination energies from the CB2 to the VB in the allowed regions are above ∼3.5 eV, in good agreement with the experimental observation (dashed ellipses in Fig. 1) that the angular shift occurs at around 3.5 eV. We have thus established that the HHG spectrum carries direct information on the vectorial character of the

recombination dipoles, in addition to the band structure information. We note that for the highest-order parallel even harmonics at 4.5 eV in Fig. 1 for 3.4 μm and 4.4 μm, the minima at $\alpha = 60°$ cannot be explained in terms of the DS or our three-band model, and we attribute these to interference effects from even higher conduction bands that are beyond the scope of this Letter.

Our combined experimental observations and theoretical analysis indicate the contributions of higher conduction bands to the HHG spectra from monolayer MoS_2 that goes beyond pure considerations of DS properties of the crystal and laser field. This was achieved by experimentally measuring the harmonics polarized parallel and perpendicular to the driving laser polarization for three different wavelengths, aided by careful theoretical analysis that selects the contributions from different recombination dipoles. The experimental signature manifests in the parallel-polarized harmonics below (above) 3.5 eV being favorably emitted when the laser polarization is along the armchair (zigzag) direction, and is observed at all three wavelengths used in the experiment. Our Letter elucidates the novel interplay between the DSs of the system and material-specific properties. We believe that our results aid in the fundamental understanding of light-matter interactions in TMDs, and may enable HHG spectroscopy of not only the band structure [31], but also the vectorial nature of the transition dipoles [32] beyond a two-band description, as well as electron-hole recombinations from different conduction bands in other materials.

L. Y. and M. B. G. acknowledge support from the National Science Foundation, under Grants No. PHY-1713671 and No. PHY-2110317, and high performance computational resources provided by the Louisiana Optical Network Infrastructure. R. H. acknowledges support by the Alexander von Humboldt Foundation. B. N. acknowledges support by the National Science Foundation Graduate Research Fellowship Program. M. Z. acknowledges support by the Federal Ministry of Education and Research (BMBF) under "Make our Planet Great Again —German Research Initiative" (Grant No. 57427209 "QUESTforENERGY") implemented by DAAD. M. Z. acknowledges funding by the W. M. Keck Foundation, funding from the UC Office of the President within the Multicampus Research Programs and Initiatives (M21PL3263), and funding from Laboratory Directed Research and Development Program at Berkeley Lab (107573). Z. G., E. N., A. G., and A. T. acknowledge support by DFG Collaborative Research Center SFB 1375 "NOA" Project B2, and thank Stephanie Höppener and Ulrich S. Schubert for enabling our Raman spectroscopy study at the JCSM. D. K. acknowledges support by DFG Collaborative Research Center SFB 1375 "NOA" Project C4. D. Y. Q. was supported by the U.S. Department of Energy, Office of Science, Office of Basic Energy Sciences Early Career Research Program under Award No. DE-SC0021965.

L. Y. and R. H. contributed equally to this work.

*richard.hollinger1@gmail.com
†mwz@berkeley.edu

[1] G. Vampa and T. Brabec, Merge of high harmonic generation from gases and solids and its implications for attosecond science, J. Phys. B **50**, 083001 (2017).
[2] S. Y. Kruchinin, F. Krausz, and V. S. Yakovlev, Colloquium: Strong-field phenomena in periodic systems, Rev. Mod. Phys. **90**, 021002 (2018).
[3] S. Ghimire and D. A. Reis, High-harmonic generation from solids, Nat. Phys. **15**, 10 (2019).
[4] M. R. Bionta, E. Haddad, A. Leblanc, V. Gruson, P. Lassonde, H. Ibrahim, J. Chaillou, N. Émond, M. R. Otto, A. Jiménez-Galán, R. E. F. Silva, M. Ivanov, B. J. Siwick, M. Chaker, and F. Légaré, Tracking ultrafast solid-state dynamics using high harmonic spectroscopy, Phys. Rev. Res. **3**, 023250 (2021).
[5] H. Liu, Y. Li, Y. S. You, S. Ghimire, T. F. Heinz, and D. A. Reis, High-harmonic generation from an atomically thin semiconductor, Nat. Phys. **13**, 262 (2017).
[6] T. T. Luu and H. J. Wörner, Measurement of the berry curvature of solids using high-harmonic spectroscopy, Nat. Commun. **9**, 916 (2018).
[7] R. E. F. Silva, I. V. Blinov, A. N. Rubtsov, O. Smirnova, and M. Ivanov, High-harmonic spectroscopy of ultrafast many-body dynamics in strongly correlated systems, Nat. Photonics **12**, 266 (2018).
[8] Y. Murakami, S. Takayoshi, A. Koga, and P. Werner, High-harmonic generation in one-dimensional mott insulators, Phys. Rev. B **103**, 035110 (2021).
[9] C. Orthodoxou, A. Zaïr, and G. H. Booth, High harmonic generation in two-dimensional mott insulators, npj Quantum Mater. **6**, 76 (2021).
[10] Simon Vendelbo Bylling Jensen and L. B. Madsen, Edge-state and bulklike laser-induced correlation effects in high-harmonic generation from a linear chain, Phys. Rev. B **104**, 054309 (2021).
[11] Y. Bai, F. Fei, S. Wang, N. Li, X. Li, F. Song, R. Li, Z. Xu, and P. Liu, High-harmonic generation from topological surface states, Nat. Phys. **17**, 311 (2021).
[12] C. P. Schmid, L. Weigl, P. Grössing, V. Junk, C. Gorini, S. Schlauderer, S. Ito, M. Meierhofer, N. Hofmann, D. Afanasiev, J. Crewse, K. A. Kokh, O. E. Tereshchenko, J. Güdde, F. Evers, J. Wilhelm, K. Richter, U. Höfer, and R. Huber, Tunable non-integer high-harmonic generation in a topological insulator, Nature (London) **593**, 385 (2021).
[13] D. Baykusheva, A. Chacón, D. Kim, D. E. Kim, D. A. Reis, and S. Ghimire, Strong-field physics in three-dimensional topological insulators, Phys. Rev. A **103**, 023101 (2021).
[14] G. Vampa, C. R. McDonald, G. Orlando, D. D. Klug, P. B. Corkum, and T. Brabec, Theoretical Analysis of High-Harmonic Generation in Solids, Phys. Rev. Lett. **113**, 073901 (2014).

[15] I. Floss, C. Lemell, G. Wachter, V. Smejkal, S. A. Sato, X.-M. Tong, K. Yabana, and J. Burgdörfer, *Ab initio* multiscale simulation of high-order harmonic generation in solids, Phys. Rev. A **97**, 011401(R) (2018).
[16] L. Yue and M. B. Gaarde, Imperfect Recollisions in High-Harmonic Generation in Solids, Phys. Rev. Lett. **124**, 153204 (2020).
[17] N. Yoshikawa, K. Nagai, K. Uchida, Y. Takaguchi, S. Sasaki, Y. Miyata, and K. Tanaka, Interband resonant high-harmonic generation by valley polarized electron-hole pairs, Nat. Commun. **10**, 3709 (2019).
[18] J. Cao, F. Li, Y. Bai, P. Liu, and R. Li, Inter-half-cycle spectral interference in high-order harmonic generation from monolayer mos2, Opt. Express **29**, 4830 (2021).
[19] C. Liu, Y. Zheng, Z. Zeng, and R. Li, Polarization-resolved analysis of high-order harmonic generation in monolayer MoS2, New J. Phys. **22**, 073046 (2020).
[20] M. Guan, S. Hu, H. Zhao, C. Lian, and S. Meng, Toward attosecond control of electron dynamics in two-dimensional materials, Appl. Phys. Lett. **116**, 043101 (2020).
[21] Y. Kobayashi, C. Heide, H. K. Kelardeh, A. Johnson, F. Liu, T. F. Heinz, D. A. Reis, and S. Ghimire, Polarization flipping of even-order harmonics in monolayer transition-metal dichalcogenides, Ultrafast Sci. **2021**, 9820716 (2021).
[22] C. Heide, Y. Kobayashi, A. C. Johnson, F. Liu, T. F. Heinz, D. A. Reis, and S. Ghimire, Probing electron-hole coherence in strongly driven 2d materials using high-harmonic generation, Optica **9**, 512 (2022).
[23] S. Manzeli, D. Ovchinnikov, D. Pasquier, O. V. Yazyev, and A. Kis, 2d transition metal dichalcogenides, Nat. Rev. Mater. **2**, 17033 (2017).
[24] I. Kilen, M. Kolesik, J. Hader, J. V. Moloney, U. Huttner, M. K. Hagen, and S. W. Koch, Propagation Induced Dephasing in Semiconductor High-Harmonic Generation, Phys. Rev. Lett. **125**, 083901 (2020).
[25] M. Hussain, S. Kaassamani, T. Auguste, W. Boutu, D. Gauthier, M. Kholodtsova, J.-T. Gomes, L. Lavoute, D. Gaponov, N. Ducros, S. Fevrier, R. Nicolas, T. Imran, P. Zeitoun, G. O. Williams, M. Fajardo, and H. Merdji, Spectral control of high order harmonics through nonlinear propagation effects, Appl. Phys. Lett. **119**, 071101 (2021).
[26] O. Neufeld, D. Podolsky, and O. Cohen, Floquet group theory and its application to selection rules in harmonic generation, Nat. Commun. **10**, 405 (2019).
[27] T. T. Luu and H. J. Wörner, High-order harmonic generation in solids: A unifying approach, Phys. Rev. B **94**, 115164 (2016).
[28] N. Klemke, N. Tancogne-Dejean, G. M. Rossi, Y. Yang, F. Scheiba, R. E. Mainz, G. Di Sciacca, A. Rubio, F. X. Kärtner, and O. D. Mücke, Polarization-state-resolved high-harmonic spectroscopy of solids, Nat. Commun. **10**, 1319 (2019).
[29] F. Langer, M. Hohenleutner, U. Huttner, S. W. Koch, M. Kira, and R. Huber, Symmetry-controlled temporal structure of high-harmonic carrier fields from a bulk crystal, Nat. Photonics **11**, 227 (2017).
[30] S. Jiang, S. Gholam-Mirzaei, E. Crites, J. E. Beetar, M. Singh, R. Lu, M. Chini, and C. D. Lin, Crystal symmetry and polarization of high-order harmonics in zno, J. Phys. B **52**, 225601 (2019).
[31] G. Vampa, T. J. Hammond, N. Thiré, B. E. Schmidt, F. Légaré, C. R. McDonald, T. Brabec, D. D. Klug, and P. B. Corkum, All-Optical Reconstruction of Crystal Band Structure, Phys. Rev. Lett. **115**, 193603 (2015).
[32] K. Uchida, V. Pareek, K. Nagai, K. M. Dani, and K. Tanaka, Visualization of two-dimensional transition dipole moment texture in momentum space using high-harmonic generation spectroscopy, Phys. Rev. B **103**, L161406 (2021).
[33] G. Vampa, T. J. Hammond, N. Thiré, B. E. Schmidt, F. Légaré, C. R. McDonald, T. Brabec, and P. B. Corkum, Linking high harmonics from gases and solids, Nature (London) **522**, 462 (2015).
[34] S. Jiang, J. Chen, H. Wei, C. Yu, R. Lu, and C. D. Lin, Role of the Transition Dipole Amplitude and Phase on the Generation of Odd and Even High-Order Harmonics in Crystals, Phys. Rev. Lett. **120**, 253201 (2018).
[35] P. G. Hawkins, M. Y. Ivanov, and V. S. Yakovlev, Effect of multiple conduction bands on high-harmonic emission from dielectrics, Phys. Rev. A **91**, 013405 (2015).
[36] M. Wu, D. A. Browne, K. J. Schafer, and M. B. Gaarde, Multilevel perspective on high-order harmonic generation in solids, Phys. Rev. A **94**, 063403 (2016).
[37] T. Ikemachi, Y. Shinohara, T. Sato, J. Yumoto, M. Kuwata-Gonokami, and K. L. Ishikawa, Trajectory analysis of high-order-harmonic generation from periodic crystals, Phys. Rev. A **95**, 043416 (2017).
[38] T.-Y. Du, D. Tang, X.-H. Huang, and X.-B. Bian, Multichannel high-order harmonic generation from solids, Phys. Rev. A **97**, 043413 (2018).
[39] C. Yu, H. Iravani, and L. B. Madsen, Crystal-momentum-resolved contributions to multiple plateaus of high-order harmonic generation from band-gap materials, Phys. Rev. A **102**, 033105 (2020).
[40] M. Hohenleutner, F. Langer, O. Schubert, M. Knorr, U. Huttner, S. W. Koch, M. Kira, and R. Huber, Real-time observation of interfering crystal electrons in high-harmonic generation, Nature (London) **523**, 572 (2015).
[41] G. Ndabashimiye, S. Ghimire, M. Wu, D. A. Browne, K. J. Schafer, M. B. Gaarde, and D. A. Reis, Solid-state harmonics beyond the atomic limit, Nature (London) **534**, 520 (2016).
[42] A. J. Uzan, G. Orenstein, Á. Jiménez-Galán, C. McDonald, R. E. F. Silva, B. D. Bruner, N. D. Klimkin, V. Blanchet, T. Arusi-Parpar, M. Krüger, A. N. Rubtsov, O. Smirnova, M. Ivanov, B. Yan, T. Brabec, and N. Dudovich, Attosecond spectral singularities in solid-state high-harmonic generation, Nat. Photonics **14**, 183 (2020).
[43] A. George, C. Neumann, D. Kaiser, R. Mupparapu, T. Lehnert, U. Hübner, Z. Tang, A. Winter, U. Kaiser, I. Staude, and A. Turchanin, Controlled growth of transition metal dichalcogenide monolayers using knudsen-type effusion cells for the precursors, J. Phys. Mater.**2**, 016001 (2019).
[44] S. Shree, A. George, T. Lehnert, C. Neumann, M. Benelajla, C. Robert, X. Marie, K. Watanabe, T. Taniguchi, U. Kaiser, B. Urbaszek, and A. Turchanin, High optical quality of mos 2 monolayers grown by chemical vapor deposition, 2D Mater. **7**, 015011 (2019).

[45] C. Lee, H. Yan, L. E. Brus, T. F. Heinz, J. Hone, and S. Ryu, Anomalous lattice vibrations of single- and few-layer mos2, ACS Nano **4**, 2695 (2010).

[46] See Supplemental Material at http://link.aps.org/supplemental/10.1103/PhysRevLett.129.147401 for additional details on the material characterization, the HHG experimental setup, and simulation details.

[47] L. Jia, Z. Zhang, D. Z. Yang, Y. Liu, M. S. Si, G. P. Zhang, and Y. S. Liu, Optical high-order harmonic generation as a structural characterization tool, Phys. Rev. B **101**, 144304 (2020).

[48] Note that the angular dependence of each harmonic has been measured in separate scans so that the direct comparison, on a linear scale, of the yield of different harmonics is less meaningful than the direct comparison of the yield of one harmonic at different angles (see SM [46]).

[49] K. Kaneshima, Y. Shinohara, K. Takeuchi, N. Ishii, K. Imasaka, T. Kaji, S. Ashihara, K. L. Ishikawa, and J. Itatani, Polarization-Resolved Study of High Harmonics from Bulk Semiconductors, Phys. Rev. Lett. **120**, 243903 (2018).

[50] In calculations, the corresponding electric field of 2.07×10^{-3} a.u. yields the best match to the experimental harmonic cutoff energies, and is consistent with a reduction of the electric field amplitude at the air-MoS_2 interface in combination with focal-volume averaging.

[51] L. Yue and M. B. Gaarde, Introduction to theory of high-harmonic generation in solids: Tutorial, J. Opt. Soc. Am. B **39**, 535 (2022).

[52] D. Golde, T. Meier, and S. W. Koch, High harmonics generated in semiconductor nanostructures by the coupled dynamics of optical inter- and intraband excitations, Phys. Rev. B **77**, 075330 (2008).

[53] O. Schubert, M. Hohenleutner, F. Langer, B. Urbanek, C. Lange, U. Huttner, D. Golde, T. Meier, M. Kira, S. W. Koch, and R. Huber, Sub-cycle control of terahertz high-harmonic generation by dynamical bloch oscillations, Nat. Photonics **8**, 119 (2014).

[54] L. Yue and M. B. Gaarde, Structure gauges and laser gauges for the semiconductor bloch equations in high-order harmonic generation in solids, Phys. Rev. A **101**, 053411 (2020).

[55] K. S. Virk and J. E. Sipe, Semiconductor optics in length gauge: A general numerical approach, Phys. Rev. B **76**, 035213 (2007).

[56] G.-B. Liu, W.-Y. Shan, Y. Yao, W. Yao, and D. Xiao, Three-band tight-binding model for monolayers of group-vib transition metal dichalcogenides, Phys. Rev. B **88**, 085433 (2013).

[57] T. G. Pedersen, K. Pedersen, and T. B. Kriestensen, Optical matrix elements in tight-binding calculations, Phys. Rev. B **63**, 201101(R) (2001).

[58] The angular yield is taken as the integrated yield of width $0.4\omega_0$ around a harmonic, with ω_0 the fundamental photon energy.

[59] L. Yue and M. B. Gaarde, Expanded view of electron-hole recollisions in solid-state high-order harmonic generation: Full-brillouin-zone tunneling and imperfect recollisions, Phys. Rev. A **103**, 063105 (2021).

[60] F. Bloch, Über die quantenmechanik der elektronen in kristallgittern, Z. Phys. **52**, 555 (1929).